Conclusions

The present study demonstrated that cerebral hyperperfusion after CEA results in postoperative cerebral white matter damage that correlates with postoperative cognitive impairment.

Disclosure Statement

The authors declare that they have no conflict of interest.

References

1 Piepgras DG, Morgan MK, Sundt TM Jr, Yanagihara T, Mussman LM: Intracerebral hemorrhage after carotid endarterectomy. J Neurosurg 1988;68:532–536.
2 Sundt TM Jr, Sharbrough FW, Piepgras DG, Kearns TP, Messick JM Jr, O'Fallon WM: Correlation of cerebral blood flow and electroencephalographic changes during carotid endarterectomy, with results of surgery and hemodynamics of cerebral ischemia. Mayo Clin Proc 1981;56:533–543.
3 Solomon RA, Loftus CM, Quest DO, Correll JW: Incidence and etiology of intracerebral hemorrhage following carotid endarterectomy. J Neurosurg 1986;64:29–34.
4 Jansen C, Sprengers AM, Moll FL, Vermeulen FE, Hamerlijnck RP, van Gijn J, Ackerstaff RG: Prediction of intracerebral haemorrhage after carotid endarterectomy by clinical criteria and intraoperative transcranial Doppler monitoring: results of 233 operations. Eur J Vasc Surg 1994;8:220–225.
5 Ogasawara K, Sakai N, Kuroiwa T, Hosoda K, Iihara K, Toyoda K, Sakai C, Nagata I, Ogawa A: Intracranial hemorrhage associated with cerebral hyperperfusion syndrome following carotid endarterectomy and carotid artery stenting: retrospective review of 4,494 patients. J Neurosurg 2007;107:1130–1136.
6 Ogasawara K, Yukawa H, Kobayashi M, Mikami C, Konno H, Terasaki K, Inoue T, Ogawa A: Prediction and monitoring of cerebral hyperperfusion after carotid endarterectomy by using single-photon emission computerized tomography scanning. J Neurosurg 2003;99:504–510.
7 Hirooka R, Ogasawara K, Sasaki M, Yamadate K, Kobayashi M, Suga Y, Yoshida K, Otawara Y, Inoue T, Ogawa A: Magnetic resonance imaging in patients with cerebral hyperperfusion and cognitive impairment following carotid endarterectomy. J Neurosurg 2008;108:1178–1183.
8 Ogasawara K, Yamadate K, Kobayashi M, Endo H, Fukuda T, Yoshida K, Terasaki K, Inoue T, Ogawa A: Postoperative cerebral hyperperfusion associated with impaired cognitive function in patients undergoing carotid endarterectomy. J Neurosurg 2005;102:38–44.
9 Schiavone F, Charlton RA, Barrick TR, Morris RG, Markus HS: Imaging age-related cognitive decline: a comparison of diffusion tensor and magnetization transfer MRI. J Magn Reson Imag 2009;29:23–30.
10 Basser PJ: Inferring microstructural features and the physiological state of tissues from diffusion-weighted images. NMR Biomed 1995;8:333–344.
11 Beaulieu C: The basis of anisotropic water diffusion in the nervous system: a technical review. NMR Biomed 2002;15:435–455.
12 O'Sullivan M, Morris RG, Huckstep B, Jones DK, Williams SC, Markus HS: Diffusion tensor MRI correlates with executive dysfunction in patients with ischaemic leukoaraiosis. J Neurol Neurosurg Psychiatry 2004;75:441–447.
13 Kraus MF, Susmaras T, Caughlin BP, Walker CJ, Sweeney JA, Little DM: White matter integrity and cognition in chronic traumatic brain injury: a diffusion tensor imaging study. Brain 2007;130:2508–2519.
14 Stebbins GT, Murphy CM: Diffusion tensor imaging in Alzheimer's disease and mild cognitive impairment. Behav Neurol 2009;21:39–49.
15 Ogasawara K, Ito H, Sasoh M, Okuguchi T, Kobayashi M, Yukawa H, Terasaki K, Ogawa A: Quantitative measurement of regional cerebrovascular reactivity to acetazolamide using [^{123}I]iodoamphetamine autoradiographic method with single photon emission computed tomography: validation study using [^{15}O]H_2O positron emission tomography. J Nucl Med 2003;44:520–525.
16 Iida H, Itoh H, Nakazawa M, Hatazawa J, Nishimura H, Onishi Y, Uemura K: Quantitative mapping of regional cerebral blood flow using iodine-123-IMP and SPECT. J Nucl Med 1994;35:2019–2030.
17 Friston KJ, Frith CD, Liddle PF, Dolan RJ, Lammertsma AA, Frackowiak RS: The relationship between global and local changes in PET scans. J Cereb Blood Flow Metab 1990;10:458–466.
18 Takeuchi R, Matsuda H, Yoshioka K, Yonekura Y: Cerebral blood flow SPET in transient global amnesia with automated ROI analysis by 3DSRT. Eur J Nucl Med Mol Imaging 2004;31:578–589.
19 Abe O, Takao H, Gonoi W, Sasaki H, Murakami M, Kabasawa H, Kawaguchi H, Goto M, Yamada H, Yamasue H, Kasai K, Aoki S, Ohtomo K: Voxel-based analysis of the diffusion tensor. Neuroradiology 2010;52:669–710.
20 Jones DK, Symms MR, Cercignani M, Howard RJ: The effect of filter size on VBM analyses of DT-MRI data. NeuroImage 2005;26:546–554.
21 Shinagawa F, Kobayashi S, Fujita K: Japanese Wechsler Adult Intelligence Scale-Revised. Tokyo, Nihon Bunka Kagakusha, 1990.
22 Koyama M: Clinical Psychology of Brain Damage. Tokyo, Gakuen Sha, 1985, pp 48–54.
23 Lezak MD: Neuropsychological Assessment, ed 3. New York, Oxford University Press, 1995.
24 Otawara Y, Ogasawara K, Ogawa A, Yamadate K: Cognitive function before and after surgery in patients with unruptured intracranial aneurysm. Stroke 2005;36:142–143.
25 Arnold M, Sturzenegger M, Schäffler L, Seiler RW: Continuous intraoperative monitoring of middle cerebral artery blood flow velocities and electroencephalography during carotid endarterectomy: a comparison of the two methods to detect cerebral ischemia. Stroke 1997;28:1345–1350.
26 Karapanayiotides T, Meuli R, Devuyst G, Piechowski-Jozwiak B, Dewarrat A, Ruchat P, Von Segesser L, Bogousslavsky J: Postcarotid endarterectomy hyperperfusion or reperfusion syndrome. Stroke 2005;36:21–26.
27 Smith JL, Evans DH, Fan L, Gaunt ME, London NJ, Bell PR, Naylor AR: Interpretation of embolic phenomena during carotid endarterectomy. Stroke 1995;26:2281–2284.
28 Wolf O, Heider P, Heinz M, Poppert H, Sander D, Greil O, Weiss W, Hanke M, Eckstein HH: Microembolic signals detected by transcranial Doppler sonography during carotid endarterectomy and correlation with serial diffusion-weighted imaging. Stroke 2004;35:e373–e375.
29 Heyer EJ, Sharma R, Rampersad A, Winfree CJ, Mack WJ, Solomon RA, Todd GJ, McCormick PC, McMurtry JG, Quest DO, Stern Y, Lazar RM, Connolly ES: A controlled prospective study of neuropsychological dysfunction following carotid endarterectomy. Arch Neurol 2002;59:217–222.

30 Le Bihan D, Poupon C, Amadon A, Lethimonnier F: Artifacts and pitfalls in diffusion MRI. J Magn Reson Imaging 2006;24:478–488.
31 Alexander AL, Lee JE, Wu YC, Field AS: Comparison of diffusion tensor imaging measurements at 3.0 T versus 1.5 T with and without parallel imaging. Neuroimage Clin North Am 2006;16:299–309.
32 Ardekani S, Shinha U: Geometric distortion correction of high-resolution 3 T diffusion brain images. Magn Reson Med 2005;54:1163–1171.
33 Bammer R, Auer M, Keeling SL, Augustin M, Stables LA, Prokesch RW, Stollberger R, Moseley ME, Fazekas F: Diffusion tensor imaging using single-shot SENSE-EPI. Magn Reson Med 2002;48:128–136.
34 Jaermann T, Crelier G, Pruessmann KP, Golay X, Netsch T, van Muiswinkel AM, Mori S, van Zijl PC, Valavanis A, Kollias S, Boesiger P: SENSE-DTI at 3 T. Magn Reson Med 2004;51:230–236.
35 Fushimi Y, Miki Y, Okada T, Yamamoto A, Mori N, Hanakawa T, Urayama S, Aso T, Fukuyama H, Kikuta K, Togashi K: Fractional anisotropy and mean diffusivity: comparison between 3.0-T and 1.5-T diffusion tensor imaging with parallel imaging using histogram and region of interest analysis. NMR Biomed 2007;20:743–748.
36 Yamamoto A, Miki Y, Urayama S, Fushimi Y, Okada T, Hanakawa T, Fukuyama H, Togashi K: Diffusion tensor fiber tractography of the optic radiation: analysis with 6-, 12-, 40-, and 81-directional motion-probing gradients, a preliminary study. AJNR Am J Neuroradiol 2007;28:92–96.
37 Bruno S, Cercignani M, Ron MA: White matter abnormalities in bipolar disorder: a voxel-based diffusion tensor imaging study. Bipolar Disord 2008;10:460–468.
38 Van Hecke W, Leemans A, De Backer S, Jeurissen B, Parizel PM, Sijbers J: Comparing isotropic and anisotropic smoothing for voxel-based DTI analyses: a simulation study. Hum Brain Mapp 2010;31:98–114.

Clinical Anatomy 25:969–972 (2012)

COMPENDIUM OF ANATOMICAL VARIANTS

Rare Coronary Anastomoses Between the Aorta, Pulmonary Trunk, Left Coronary Artery, and Subclavian Artery

MASAKI TAKECHI,* JUN YAN, AND JIRO HITOMI

Division of Human Embryology, Department of Anatomy, Iwate Medical University, Iwate, Japan

We report a rare case of coronary anastomoses in an 83-year-old male cadaveric heart. Anomalous vessels arose from the right sinus of the aorta, left main coronary artery, left anterior descending artery, left anterior medial atrial artery, and left subclavian artery. These vessels bifurcated and anastomosed, and finally connected to the pulmonary trunk. The present case is categorized as a multilateral coronary artery fistula in cardiology. Clin. Anat. 25:969–972, 2012. © 2012 Wiley Periodicals, Inc.

Key words: coronary anastomosis; pulmonary trunk; coronary artery fistula

CASE REPORT

During the 2011 gross anatomy course at Iwate Medical University, a rare case of coronary anastomoses was detected in the heart of an 83-year-old male cadaver who had died of ascending colon cancer (Figs. 1A and 2A). The heart showed a tortuous and dilated connection between the aorta and pulmonary trunk (PT), with smaller anastomoses with the left coronary artery (LCA) branches and left subclavian artery (LSA). On the right side of the heart, we identified a vessel with dilatation proceeding from the right sinus of the aorta (RSA; Fig. 1B, branch 1). The orifice was very close to the origin of the right coronary artery (RCA; Fig. 1C and 1D). It passed tortuously and bifurcated (Fig. 1B, arrow) on the wall of the PT. These two vessels anastomosed and finally connected to the anterior sinus of the PT (Figs. 1B and 2B, dark gray; Fig. 2C and 2D) with a large dilatation (Figs. 1B and 2B, asterisk). On the left side of the heart, we identified anomalous vessels arising from the LCA and LSA which connected to the PT. Four vessels were given off by the LCA: one from the left main coronary artery (Fig. 2B, branch 2), two from the left anterior descending artery (Fig. 2B, branches 3 and 4), and one from the left anterior medial atrial artery (Fig. 2B, branch 5). These branches bifurcated and anastomosed, and finally connected to the PT (Fig. 2B–2D). Moreover, we identified an anomalous connection between the LSA and PT (Figs. 1B and 2B, branch 6). A vessel was connected to branch 6 on the PT (Figs. 1B and 2B, branch 7); however, this vessel was accidentally cut during dissection, and the origin was unclear.

There were no anomalous origins or distributions in other branches of the coronary arteries such as the RCA (this artery gave off the posterior interventricular branch), the median artery, and the circumflex branch of the LCA (Figs. 1A, 1B, 2A, and 2B). Additionally, there were no other anomalies inside the heart, such as defects of the interatrial septum.

DISCUSSION

Anastomosis of a coronary artery and a cardiac chamber or vessel is an abnormal condition, and majority of such cases are caused by congenital malformations. In cardiology, such an anastomosis is called a coronary artery fistula (CAF). CAF is a rare anomaly, with an incidence of 0.02%–2.1% in an adult angiographic series (Vavuranakis et al., 1995; Nawa

*Correspondence to: Masaki Takechi, Division of Human Embryology, Department of Anatomy, Iwate Medical University 2-1-1, Nishitokuta, Yahaba-cho, Shiwa-gun, Iwate 028-3694, Japan. E-mail: takechi@iwate-med.ac.jp

Received 15 May 2012; Revised 2 July 2012; Accepted 5 July 2012

Published online 7 August 2012 in Wiley Online Library (wileyonlinelibrary.com). DOI 10.1002/ca.22141

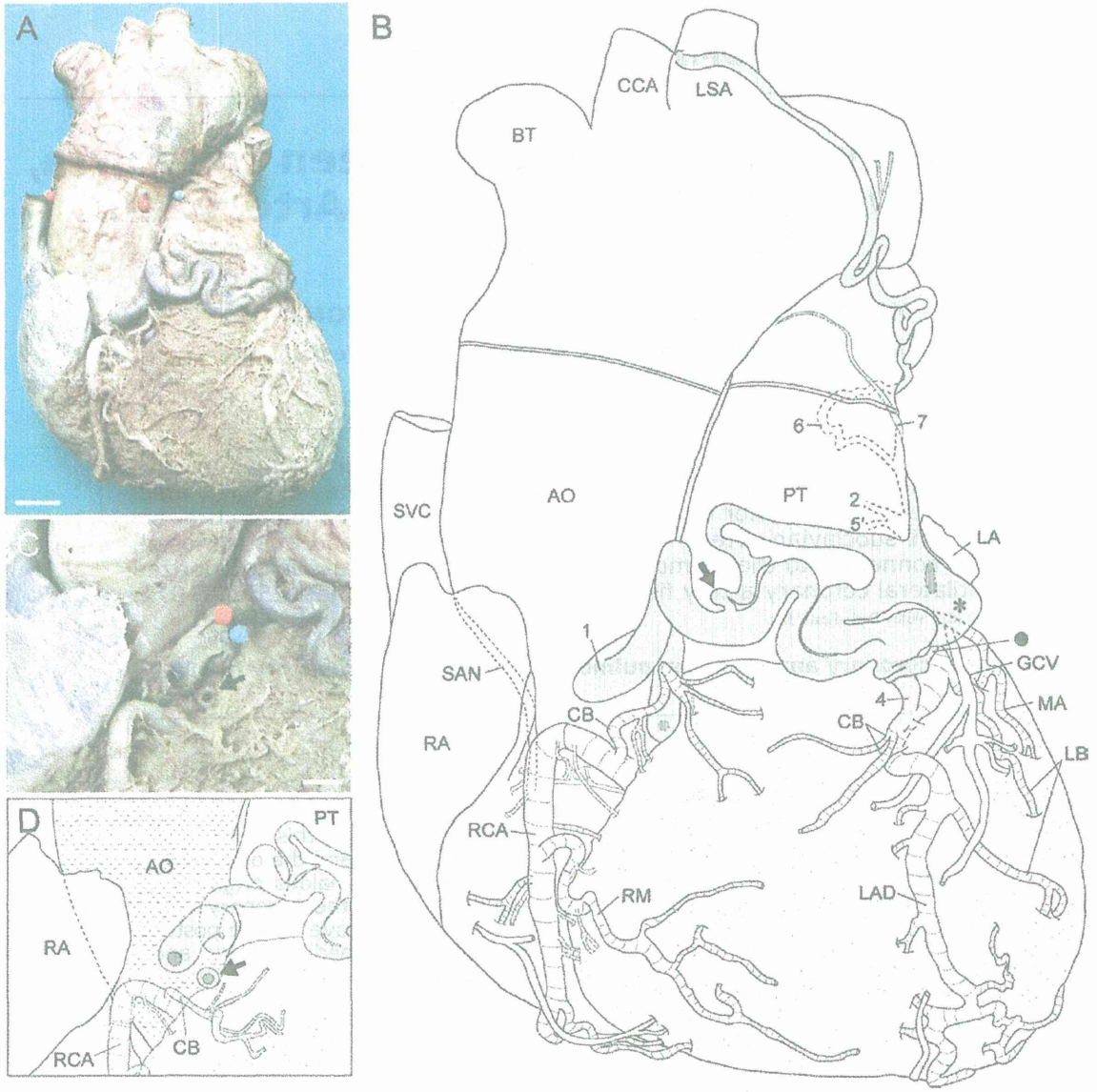

Fig. 1. Anterior view of the heart showing rare coronary anastomoses. **A**: Photograph of the anterior view of the heart. **B**: Schematic representation of (A). The anomalous anastomoses are indicated in light gray. Arabic numerals indicate anomalous vessels arising from the aorta (AO) or LCA. Detailed courses of branches 2, 4, and 5′ (a bifurcated vessel of branch 5) are illustrated in Figure 2B. Black circles in Figures 1 and 2 show the same vessel. Double lines on the AO and the PT indicate cutoff lines in the dissection process. **C**: Magnified image of the hatched box shown in (A). Branch 1 was cut near its origin from the AO and moved upward to show the lumen. (D) Schematic representation of (C). Scale bars: 2 cm (A) or 1 cm (C). Abbreviations: AO, aorta; BT, brachiocephalic trunk; CB, conus branch; CCA, common carotid artery; GCV, great cardiac vein; LA, left auricle; LAD, left anterior descending artery; LB, lateral branch; LSA, left subclavian artery; MA, median artery; PT, pulmonary trunk; RA, right atrium; RCA, right coronary artery; RM, right marginal branch; SAN, sino-atrial node branch; SVC, superior vena cava.

et al., 1996; Said et al., 1998; Yener and Yener, 2001; Sercelik et al., 2003). Based on the number of donor vessels from the coronary artery, CAFs are categorized as unilateral (one vessel), bilateral (two vessels), or multilateral (three or more vessels). Multilateral CAF is very rare and accounts for only 2% of all CAF cases (Said, 2011). Interestingly, bilateral or multilateral CAFs connect more frequently to the PT than to the other sites (Levin et al., 1978; Baim et al., 1982; Said, 2011), sug-

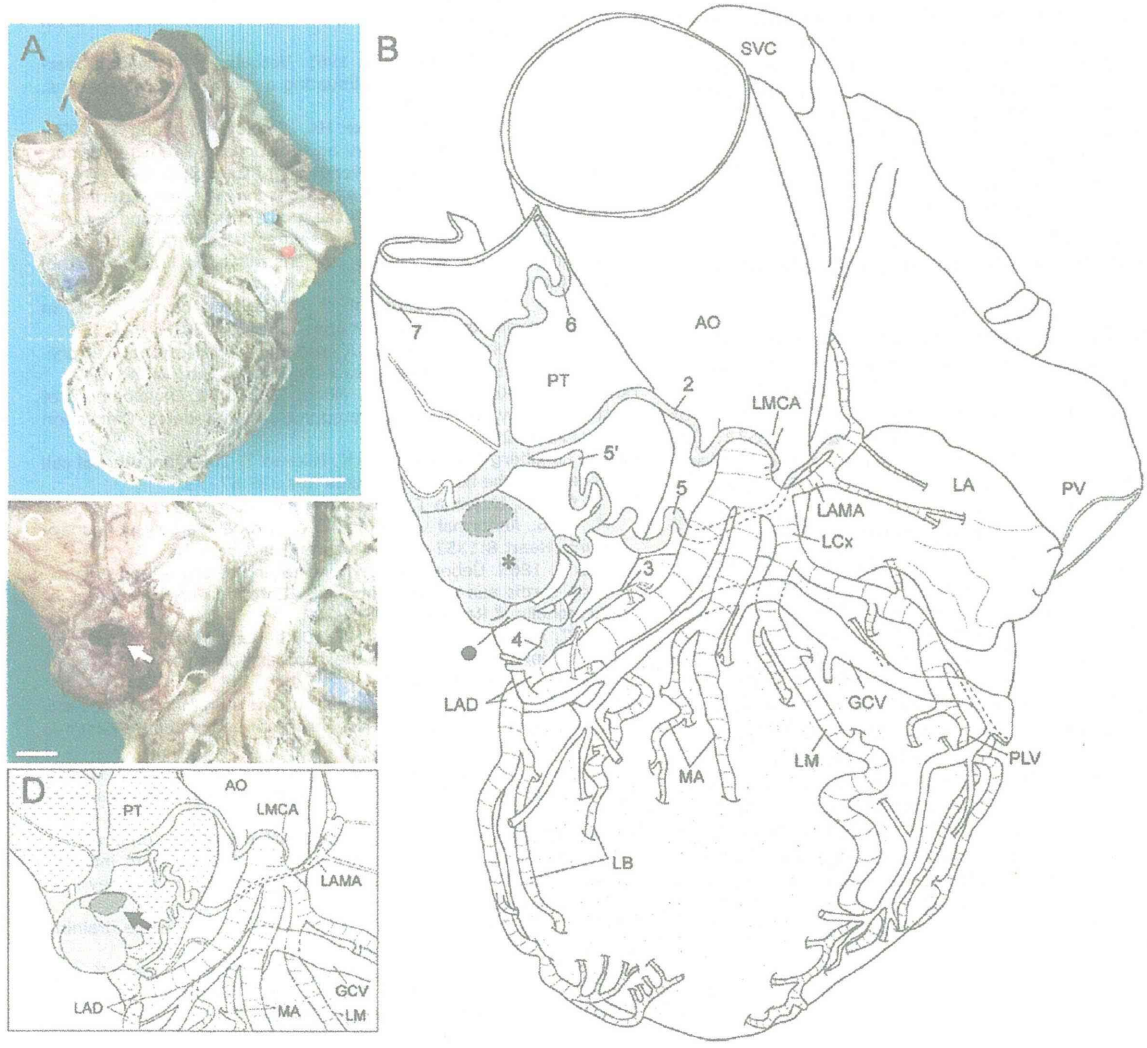

Fig. 2. Left side view of the heart showing anomalous vessels, which connect the LCA, left cubclavian artery, and the PT. The upper regions of the aorta (AO) and PT were removed at the double line in Figure 1. **A**: Photograph of the left side view of the heart. **B**: Schematic representation of (A). Arabic numerals 2–5 indicate anomalous vessels arising from vessels of the LCA. Arabic numeral 6 indicates an anastomosis between the LSA and PT (see also Fig. 1B). **C**: Magnified image of the hatched box shown in (A). The blood clot in the dilation of the vessel was removed to show the orifice at the PT (arrow). **D**: Schematic representation of (C). Scale bars: 2 cm (A) or 1 cm (C). Abbreviations: AO: aorta; GCV, great cardiac vein; LA, left auricle; LAD, left anterior descending artery; LAMA, left anterior medial atrial artery; LB, lateral branch; LCx, left circumflex artery; LM, left marginal artery; LMCA, left main coronary artery; MA, median artery; PLV, posterior left ventricular branch; PT, pulmonary trunk; PV, pulmonary vein; SVC, superior vena cava.

gesting that these anomalies have a distinct embryological basis (Baim et al., 1982). Diagnosis and clinical treatment for patients with CAF is based on the results of angiographic visualization, and hundreds of such cases have been reviewed (Said et al., 2006; Said, 2011). In contrast, only a few reports have indicated anatomical descriptions of CAF in cadaveric hearts (Krause, 1865; Brooks, 1885; Hackenseliner, 1955; Horiguchi and Koizumi, 1987).

We identified a rare case of coronary anastomoses in which six anomalous vessels arising from LCA branches, RSA, or LSA connected to the PT in a cadaveric heart (Figs. 1B and 2B, branches 1–6). This case is categorized as a multilateral CAF in cardiology. Anomalous vessels are generally given off by the coronary artery in CAFs; however, in the present case one of the vessels arose directly from the RSA not from the RCA. Only a few of such cases

have been reported to date (Moukarbel and Nasrallah, 2005; Yiginer et al., 2009; Acar et al., 2010). Furthermore, in the present case there was an anastomosis between the LSA and the PT. Brooks (1885) reported a case of multilateral CAF with anomalous connection between the RCA, LSA, aortic arch, and PT in a cadaveric heart. Despite the advent of various imaging technologies, there have been no recent reports of CAF with an anastomosis between the subclavian artery and PT (Said et al., 2006; Said, 2011). To the best of our knowledge, this is the first report of multilateral CAF involving both the RSA and LSA.

Most coronary anastomoses are congenital; however the specific nature of such entities is uncertain. Three hypotheses have been suggested regarding the embryonic origin of the anomalous connection between the coronary artery and PT: (1) vasa vasorum of the conus branch (Ernst et al., 1961), (2) anastomosis of the accessory coronary artery anlage and conus branches (Hackensellner, 1955; Gobel et al., 1970), and (3) anastomosis of the sinusoid of cardiac lumen and coronary arteries (Iwa et al., 1976). Horiguchi and Koizumi (1987) reported a case of coronary-PT anastomosis that supports the second hypothesis; however, this hypothesis was based on the suggestion that the coronary artery develops through angiogenic sprouting from the base of the aorta (Licata, 1962; Odgen, 1968; Hirakow, 1983; Conte and Pellegrini, 1984; Hutchins et al., 1988); however, this idea has not been supported by recent data (Mikawa and Gourdie, 1996). As the developmental origin of the coronary artery network is not thoroughly understood (Mikawa, 1999; Ishii et al., 2009), further detailed studies on the development of the coronary artery are required to determine the embryologic etiology of coronary anastomosis. Moreover, the embryonic origin of the anomalous anastomosis between the LSA and PT is uncertain.

ACKNOWLEDGMENTS

Authors would like to thank Dr. Salah A. M. Said (Hospital Group Twente, Netherlands) and Dr. Yukio Aizawa (Nippon Dental University, Japan) for their helpful participation in discussion. They also thank Sadanari Takahashi, Nobuhide Sasaki, and Masato Hirakawa (Iwate Medical University) for their technical support.

REFERENCES

Acar G, Koroglu S, Yiginer O, Ozturk E, Tuncer C. 2010. Bilateral coronary artery fistula originating from the right sinus of Valsalva and left circumflex artery, and draining into the pulmonary artery. Hellenic J Cardiol 51:458–459.

Baim DS, Kline H, Silverman JF. 1982. Bilateral coronary artery—Pulmonary artery fistulas. Report of five cases and review of the literature. Circulation 65:810–815.

Brooks HS. 1885. Two cases of an abnormal coronary artery of the heart arising from the pulmonary artery. With some remarks upon the effect of this anomaly in producing cirsoid dilatation of the vessels. J Anat Physiol 20:26–29.

Conte G, Pellegrini A. 1984. On the development of the coronary arteries in human embryos, stages 14–19. Anat Embryol 169:209–218.

Ernst CB, Klassen KP, Ryan JM. 1961. Vascular malformation overlying the pulmonary artery simuating a patent ductus arteriosus. Circulation 23:759–761.

Gobel FL, Anderson CF, Baltaxe HA, Amplatz K, Wang Y. 1970. Shunts between the coronary and pulmonary arteries with normal origin of the coronary arteries. Am J Cardiol 25:655–661.

Hackensellner HA. 1955. Über akzessorische, von der Arteria pulmonalis abgehende Herzgefässe und ihre Bedeutung für das Verständnis der formalen Genese des Ursprunges einer oder beider Coronarterien von der Lungenschlagader. Frankf Z Pathol 66:463–470

Hirakow R. 1983. Development of the cardiac blood vessels in staged human embryos. Acta Anat 115:220–230.

Horiguchi M, Koizumi M. 1987. A case of bilateral coronary artery-pulmonary trunk anastomosis. Acta Anat Nippon 62:343–347.

Hutchins GM, Kessler-Hanna A, Moore GW. 1988. Development of the coronary arteries in the embryonic human heart. Circulation 77:1250–1257.

Ishii Y, Langberg J, Rosborough K, Mikawa T. 2009. Endothelial cell lineages of the heart. Cell Tissue Res 335:67–73.

Iwa T, Sato H, Ueyama T, Misaki T, Muranaka Y, Shin D, Tomikawa M. 1976. Abnormal vessel traffic of coronary artery-pulmonary trunk. Heart 8:1352–1357. (article in Japanese).

Krause W. 1865. Ueber den Ursprung einer accessorischen a. coronaria cordis aus der a. pulmonalis. Coronaria cordis aus der A. Pulmonalis. Z Rat Med 24:225–227.

Levin DC, Fellows KE, Abrams HL. 1978. Hemodynamically significant primary anomalies of the coronary arteries. Angiographic aspects. Circulation 58:25–34.

Licata RH. 1962. Coronary circulation. In: Abramson DI, editor. Blood Vessels and Lymphatics. New York and London: Academic Press. p 258–261.

Mikawa T. 1999. Cardiac lineages. In: Harvey RP, Rosenthal N, editors. Heart Development. San Diego and London: Academic Press. p 19–33.

Mikawa T, Gourdie RG. 1996. Pericardial mesoderm generates a population of coronary smooth muscle cells migrating into the heart along with ingrowth of the epicardial organ. Dev Biol 174:221–232.

Moukarbel GV, Nasrallah AT. 2005. Coronary artery fistula draining into the pulmonary artery. Int J Cardiol 99:493–494.

Nawa S, Miyachi Y, Toshino N, Shiba T, Hayashi K, Tamesue K, Shimizu N. 1996. Congenital coronary artery fistulae arising from bilateral coronary arteries and emptying into both pulmonary artery and left ventricle: A rare presentation. Cardiology 87:263–266.

Ogden JA. 1968. The origin of the coronary arteries. Circulation 38 (Suppl. VI):VI–150.

Said SA. 2011. Current characteristics of congenital coronary artery fistulas in adults: A decade of global experience. World J Cardiol 3:267–277.

Said SA, Relik-van Wely L, van der Werf T. 1998. Angiographically diagnosed congenital coronary artery fistulas in an adult population. Cardiologie 5:71–73.

Said SA, Lam J, van der Werf T. 2006. Solitary coronary artery fistulas: A congenital anomaly in children and adults. A contemporary review. Congenit Heart Dis 1:63–76.

Sercelik A, Mavi A, Ayalp R, Pestamalci T, Gumusburun E, Batiraliev T. 2003. Congenital coronary artery fistulas in Turkish patients undergoing diagnostic cardiac angiography. Int J Clin Pract 57:280–283.

Vavuranakis M, Bush CA, Boudoulas H. 1995. Coronary artery fistulas in adults: incidence, angiographic characteristics, natural history. Catheter Cardiovasc Diagn 35:116–120.

Yener N, Yener A. 2001. Another cause of chest pain: Coronary artery-pulmonary artery fistulae. Int J Angiol 10:85–87.

Yiginer O, Bas S, Feray H. 2009. Demonstration of coronary-to-pulmonary fistula with MDCT and conventional angiography. Int J Cardiol 134:e126–e128.

Neuroradiology (2012) 54:1187–1194
DOI 10.1007/s00234-012-1025-9

DIAGNOSTIC NEURORADIOLOGY

Carotid plaque signal differences among four kinds of T1-weighted magnetic resonance imaging techniques: A histopathological correlation study

Ayumi Saito · Makoto Sasaki · Kuniaki Ogasawara · Masakazu Kobayashi · Jiro Hitomi · Shinsuke Narumi · Hideki Ohba · Mao Yamaguchi · Kohsuke Kudo · Yasuo Terayama

Received: 17 December 2011 / Accepted: 29 February 2012 / Published online: 17 March 2012

Abstract
Introduction Several magnetic resonance (MR) imaging techniques are used to examine atherosclerotic plaque of carotid arteries; however, the best technique for visualizing intraplaque characteristics has yet to be determined. Here, we directly compared four kinds of T1-weighted (T1W) imaging techniques with pathological findings in patients with carotid stenosis.
Methods A total of 31 patients who were candidates for carotid endarterectomy were prospectively examined using a 1.5-T MRI scanner, which produced four kinds of T1W images, including non-gated spin echo (SE), cardiac-gated black-blood (BB) fast-SE (FSE), magnetization-prepared rapid acquisition with gradient echo (MPRAGE), and source image of three-dimensional time-of-flight MR angiography (SI-MRA). The signal intensity of the carotid plaque was manually measured, and the contrast ratio (CR) against the adjacent muscle was calculated. CRs from the four imaging techniques were compared to each other and correlated with histopathological specimens.
Results CRs of the carotid plaques mainly containing fibrous tissue, lipid/necrosis, and hemorrhage were significantly different with little overlaps (range: 0.92–1.15, 1.22–1.52, and 1.55–2.30, respectively) on non-gated SE. However, BB-FSE showed remarkable overlaps among the three groups (0.89–1.10, 1.07–1.23, and 1.01–1.42, respectively). MPRAGE could discriminate fibrous plaques from hemorrhagic plaques but not from lipid/necrosis-rich plaques: (0.77–1.07, 1.45–2.43, and 0.85–1.42, respectively). SI-MRA showed the same tendencies (1.01–1.39, 1.45–2.57, and 1.12–1.39, respectively).
Conclusion Among T1W MR imaging techniques, non-gated SE images can more accurately characterize intraplaque components in patients who underwent CEA when compared with cardiac-gated BB-FSE, MPRAGE, and SI-MRA images.

Keywords Carotid stenosis · Magnetic resonance imaging · Plaque imaging · T1-weighted image · Carotid endarterectomy

A. Saito · S. Narumi · H. Ohba · M. Yamaguchi · Y. Terayama
Department of Neurology and Gerontology,
Iwate Medical University,
19-1 Uchimaru,
Morioka, Japan

M. Sasaki (✉) · K. Kudo
Institute for Biomedical Sciences, Iwate Medical University,
19-1 Uchimaru,
Morioka, Japan
e-mail: masasaki@iwate-med.ac.jp

K. Ogasawara · M. Kobayashi
Department of Neurosurgery, Iwate Medical University,
19-1 Uchimaru,
Morioka, Japan

J. Hitomi
Department of Anatomy, Iwate Medical University,
19-1 Uchimaru,
Morioka, Japan

Introduction

Atherosclerotic stenosis of the cervical carotid artery, a major cause of cerebral infarction and transient ischemic attack, is a candidate for surgical treatments such as carotid endarterectomy (CEA) and carotid artery stenting (CAS).

Embolic stroke can occur as a complication of these procedures [1, 2] and is strongly associated with vulnerable carotid plaques consisting primarily of lipid-necrotic core and/or intraplaque hemorrhage accompanied by a thin fibrous cap [3, 4]. Thus, assessment of intraplaque characteristics and prediction of unstable plaques may be crucial for minimizing perisurgical embolic stroke events. Magnetic resonance (MR) plaque imaging is widely used for this purpose, but findings of the vulnerable plaques vary among articles particularly those based on T1-weighted (T1W) imaging, which is considered to be the most useful [5]. This can be attributed to marked inter-institutional differences in imaging techniques, i.e., spin echo (SE), cardiac-gated black-blood (BB) fast SE (FSE), magnetization-prepared rapid acquisition with gradient echo (MPRAGE), source image (SI) of three-dimensional (3D) time-of-flight (TOF) MR angiography (MRA) (SI-MRA), and others [4, 6–9], as well as a lack of cross-validation among these imaging techniques. Therefore, we directly compared four kinds of T1W imaging techniques and histopathological findings in patients with carotid stenosis to elucidate which technique can most accurately predict intraplaque components.

Methods

Patients

From August 2010 to November 2011, 31 consecutive patients (30 men, one woman; age range, 54–80 years; mean age, 69.6 years) with unilateral cervical carotid stenosis who underwent CEA were prospectively examined. Twenty-five carotid stenoses were symptomatic, and 18 were on the right side. In addition, severity of the stenoses was 70–99% (mean, 87.7%) based on North American Symptomatic Carotid Endarterectomy Trial (NASCET) criteria using digital subtraction angiography. Clinical characteristics of the patients included hypertension in 22 patients, hyperlipidemia in 18, and diabetes mellitus in 14. The following drugs were administered to the patients: antiplatelet agents in 31 patients, angiotensin-2 receptor blocker in 13, statin in 13, and insulin in two. All examinations in this study were performed after obtaining approval from the institutional review board and a written informed consent from each patient.

Imaging protocol

Four kinds of axial T1W images of the affected carotid bifurcation were obtained within 1 week prior to CEA using a 1.5-T MR scanner (Echelon Vega, Hitachi Medical Corporation, Tokyo, Japan) and an eight-channel neurovascular coil. The following imaging techniques and pulse sequence parameters were used: (1) non-gated SE; repetition time (TR), 500 ms; echo time (TE), 12 ms; field of view (FOV), 18 cm; matrix size, 256×256 (pixel size, 0.35×0.35 mm after zero-fill interpolation); slice thickness, 4.0 mm with interslice gaps of 1 mm; number of slices, 9; number of excitations, 2; chemical shift selective saturation (CHESS) pulse for fat suppression; non-selective saturation pulse for blood signal suppression; self-navigated radial scan adapted from periodically rotated overlapping parallel lines with enhanced reconstruction method [10] for motion correction; and acquisition time, 6 min 46 s; (2) cardiac-gated BB-FSE; TR, 1 cardiac cycle (800–1,250 ms; median, 1,000 ms) for motion correction; TE, 12 ms; FOV, 18 cm; matrix size, 256×256; slice thickness, 4.0 mm with interslice gaps of 1 mm; number of slices, 1; CHESS pulse for fat signal suppression; double inversion recovery (IR) preparatory pulses for blood signal suppression; and acquisition time, 1 min 47 s to 3 min 13 s; (3) IR-prepared fast gradient echo (GRE) that is equivalent to MPRAGE originally introduced as direct thrombus imaging [9]; TR, 1,500 ms; TE, 5.0 ms; inversion time (TI); 660 ms for blood signal suppression; FOV, 18 cm; matrix size, 256×204; slice thickness, 2.5 mm; number of slices, 35; water excitation for fat suppression; and acquisition time, 7 min; and (4) SI-MRA; spoiled GRE, TR, 35 ms; TE, 4.4 ms; flip angle 30°; FOV, 18 cm; matrix size, 256×256; slice thickness, 2.5 mm; number of slices, 30; CHESS pulse for fat signal suppression; and acquisition time, 4 min 21 s. The section direction was carefully set as perpendicular to the long axis of carotid bifurcation on the sagittal two-dimensional phase-contrast MR angiography (2D-PC MRA), the section of BB-FSE was set at the location in which the stenosis was most severe, and the mid-sections of non-gated SE, MPRAGE, and SI-MRA were set at the identical location as that of BB-FSE.

Histological evaluation

Specimens excised from the carotid bifurcations in an en bloc fashion by one of the authors (K.O.) during CEA were provided for histological evaluation. After fixation by formaldehyde, transverse sections of the carotid bifurcations with the direction and position corresponding to those of the MR images were carefully obtained by one of the authors (J.H.) on referring to the MR images including 2D-PC-MRA in which the location of the section was indicated. Histological slices of decalcified and paraffin-embedded 7-μm-thick sections were stained by hematoxylin–eosin (HE), Masson-trichrome (MT), and antiglycophorin-A (AGP) methods.

Data and statistical analyses

For quantitative evaluation of MR imaging, the signal intensities of the carotid plaque and the adjacent sternomastoid muscle were measured at the section at which four

kinds of images were obtained. The regions of interest were manually traced three times with intervals of 3–5 days on a liquid crystal display (LCD) using the polygon cursor of a free software package (zioTerm2009, Ziosoft, Tokyo, Japan) by one of the authors (A.S.) who was blinded to the clinical and MR findings. The obtained signal intensity values were then averaged, and the contrast ratio (CR) of the carotid plaque was calculated by dividing the plaque signal intensity with the muscle signal intensity.

For quantitative assessment of the histological specimens, areas of the three components within the plaque, i.e., fibrous tissue, lipid/necrosis, or hemorrhage, were microscopically measured three times with intervals of 3–5 days using a manual tracing method and a free software package (ImageJ Ver. 1.44, National Institute of Health, Bethesda) by one of the authors (S.N.) who was blinded to the clinical and MR findings. Based on the averaged values of these measurements, the principal component of each plaque was determined when the area of one of the components was 50% or more of the total plaque area.

For statistical analyses, the Friedman test and the post hoc Wilcoxon test were used to determine differences in CRs of the carotid plaques among the four kinds of images obtained with different scanning methods. Kruskal–Wallis test and post-hoc Mann–Whitney test were used to determine differences among the three kinds of plaques with different main components. To determine the sensitivity and specificity of the images for the prediction of main intraplaque components, receiver operating characteristic (ROC) analyses were also performed. Furthermore, intraoperator agreements in quantitative measurements were assessed by calculating the intraclass correlation coefficient (ICC). The alpha level used was 0.05.

Results

Among 31 patients, three patients were excluded because of poor image quality due to remarkable motion artifacts, seven patients were excluded because no intraplaque component reached 50% of the total plaque area by the histological measurements, and the remaining 21 patients (54–80 years; mean age, 69.0 years) were subjects for further analyses. The measurements on histological specimens in these patients showed that the main component of the plaques was fibrous tissue in five cases (range, 53–95%; median, 66%), lipid/necrosis in six cases (50–81%; 58%), and hemorrhage in ten cases (50–66%; 58%).

CRs of the carotid plaques to the adjacent muscles were 0.92–2.30 (median, 1.52), 0.89–1.42 (1.13), 0.77–2.43 (1.42), and 1.01–2.57 (1.39) on the images with non-gated SE, BB-FSE, MPRAGE, and SI-MRA, respectively ($p<0.001$, Friedman test), and showed significant differences between BB-FSE and other methods ($p<0.001$ and $p=0.02$, post-hoc Wilcoxon test) as well as between MPRAGE and SI-MRA ($p=0.03$, post-hoc Wilcoxon test) (Fig. 1). CRs of the carotid plaques mainly containing fibrous tissue, lipid/necrosis, and hemorrhage based on non-gated SE were 0.92–1.15 (1.02), 1.22–1.52 (1.35), and 1.55–2.30 (1.81), respectively, and showed significant differences among these groups ($p<0.001$, Kruskal–Wallis test), as well as, between any combinations among these (fibrous-lipid/necrosis, $p=0.004$; fibrous-hemorrhage, $p=0.001$, lipid/necrosis-hemorrhage, $p<0.001$; Mann–Whitney test) (Table 1, Figs. 1, 2, 3 and 4). However, CRs of the plaques based on BB-FSE were 0.89–1.10 (1.09), 1.07–1.23 (1.10), and 1.01–1.42 (1.27), respectively, and showed less significant differences with larger overlaps ($p=0.01$, Kruskal–Wallis test; fibrous-lipid/necrosis, $p=0.33$; fibrous-hemorrhage, $p=0.008$, lipid/necrosis-hemorrhage, $p=0.03$; Mann–Whitney test) compared with CRs based on other imaging techniques (Table 1, Figs. 1, 2, 3 and 4). Furthermore, CRs of the plaques based on MPRAGE were 0.77–1.07 (0.91), 0.85–1.42 (1.10), and 1.45–2.43 (1.83), respectively; insignificant difference with a substantial overlap between the plaques with fibrous tissue and those with lipid/necrosis ($p=0.08$, Mann–Whitney test) was observed, although marked significant differences were found between the other two combinations (fibrous-hemorrhage, $p<0.001$; lipid/necrosis-hemorrhage, $p<0.001$; Mann–Whitney test) (Table 1, Figs. 1, 2, 3 and 4). SI-MRA showed similar results to MPRAGE: 1.01–1.39 (1.07), 1.12–1.39 (1.29), and 1.45–2.57 (1.87), respectively ($p<0.001$, Kruskal–Wallis test; fibrous-lipid/necrosis, $p=0.13$; fibrous-hemorrhage, $p=0.001$, lipid/necrosis-hemorrhage, $p<0.001$; Mann–Whitney test) (Figs. 1, 2, 3 and 4).

ROC analyses showed that the sensitivities and specificities for discriminating the plaques consisting mainly of lipid/necrosis or hemorrhage, from those consisting mainly of fibrous tissue, were 100% and 100% on non-gated SE with a cut off value of 1.19, 75% and 100% on cardiac-gated BB-FSE with a cut-off value of 1.11, 88% and 100% on MPRAGE with a cut off value of 1.08, and 100% and 80% on SI-MRA with a cut off value of 1.10, respectively. The ICC values for the measurements on MR images and histological specimens were 0.98–0.99 (median, 0.99) and 0.95–0.99 (median, 0.98), respectively, indicating excellent intraoperator agreements between the measurements obtained in this study.

Discussion

Several previous studies have compared findings from T1W MR plaque imaging with those from specimens obtained by CEA. In these studies, hyperintensity in the plaques tended

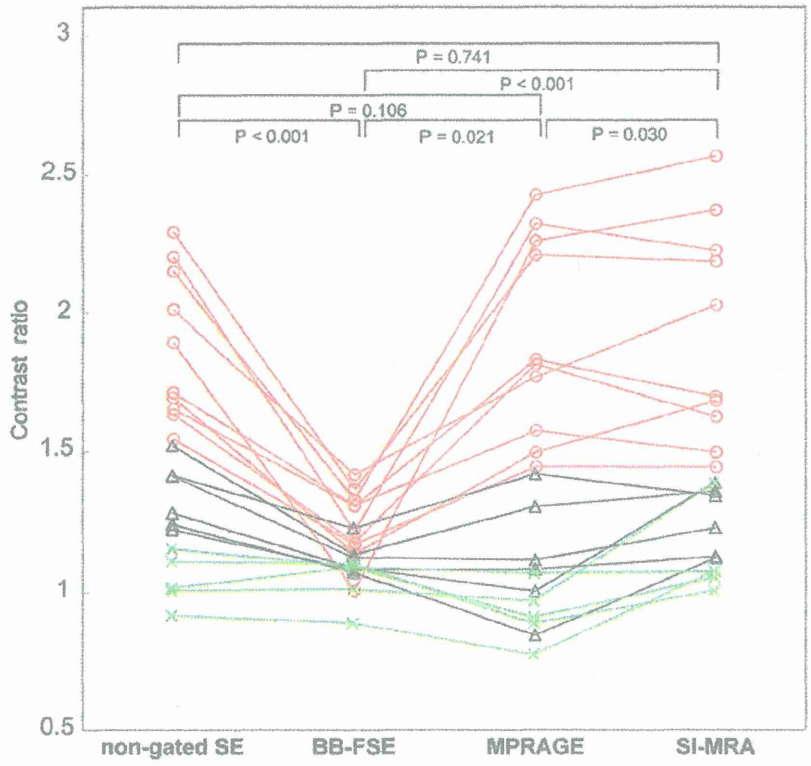

Fig. 1 Contrast ratios of the carotid plaques on T1-weighted images obtained through different imaging techniques. *SE* spin echo, *BB-FSE* black-blood fast spin echo, *MPRAGE* magnetization-prepared rapid acquisition with gradient echo, *SI-MRA* source image of three-dimensional time-of-flight MR angiography; *red lines* indicate plaques consisting mainly of hemorrhagic component, *black lines* indicate plaques consisting mainly of lipid/necrotic component, *green lines* indicate plaques consisting mainly of fibrous component; p values: Wilcoxon test. Contrast ratios (*CRs*) of the plaques to the adjacent muscles based on non-gated SE images are markedly different with little overlaps among plaques with different main components. However, CRs of the plaques based on BB-FSE are less different with marked overlaps among the groups. CRs of the plaques based on MPRAGE and SI-MRA consisting mainly of lipid/necrosis tend to overlap with those of fibrous tissue

to reflect a lipid-rich necrotic core and/or intraplaque hemorrhage, whereas isointensity to the adjacent muscle tended to reflect fibrous tissue [6–8, 11–13]. However, sensitivities and specificities for detecting vulnerable plaque components varied markedly among the studies: 56–96% and 84–94%, respectively [8, 9, 14]. In the present study, we showed substantial differences in the intraplaque contrast among different T1W plaque imaging techniques and indicated that non-gated SE is superior to BB-FSE, MPRAGE, and SI-MRA for discrimination of main intraplaque components. These results suggest that the variance in the previous studies can be attributed in part to differences in the imaging techniques used.

The cardiac-gated BB-FSE method appears to be the most popular technique for MR plaque imaging; however, in the present study, intraplaque contrast using this method

Table 1 Contrast ratios of the carotid plaque on various T1-weighted imaging techniques

	Main plaque component			Kruskal–Wallis Test (*p* values)	Mann–Whitney test (*p* values)		
	Fibrous tissue (*n*=5)	Lipid/necrosis (*n*=6)	Hemorrhage (*n*=10)		Fibrous vs. lipid/necrosis	Fibrous vs. hemorrhage	Lipid/necrosis vs. hemorrhage
Non-gated SE	0.92–1.15 (1.02)	1.22–1.52 (1.35)	1.55–2.30 (1.81)	<0.001	0.004	0.001	<0.001
Gated BB-FSE	0.89–1.10 (1.09)	1.07–1.23 (1.10)	1.01–1.42 (1.27)	0.011	0.329	0.008	0.031
MPRAGE	0.77–1.07 (0.91)	0.85–1.42 (1.10)	1.45–2.43 (1.83)	<0.001	0.082	0.001	<0.001
SI-MRA	1.01–1.39 (1.07)	1.12–1.39 (1.29)	1.45–2.57 (1.87)	<0.001	0.126	0.001	<0.001

BB-FSE black-blood fast spin–echo, *MPRAGE* magnetization-prepared rapid acquisition with gradient echo, *SE* spin–echo, *SI-MRA* source image of three-dimensional time-of-flight magnetic resonance angiography. Data are presented as range (median)